ACS APPLIED BIO MATERIALS

www.acsabm.org

Article

Sustainable Surfactant-Free Synthesis of $MnMoO_4$/Carbon Nanofiber Composite for Highly Sensitive Detection of Nimesulide in Biological and Pharmaceutical Matrices

Kumar Gokulkumar, Sakthivel Kogularasu, Shih-Hsuan Chen, Guo-Ping Chang-Chien, Wan-Ching Lin, Yung-Lung Chen,* and Kun-Mu Lee*

Cite This: *ACS Appl. Bio Mater.* 2025, 8, 8864−8879

Read Online

ACCESS | Metrics & More | Article Recommendations | Supporting Information

ABSTRACT: In this study, a high-performance electrochemical sensor based on a $MnMoO_4$/carbon nanofiber ($MnMoO_4$/CNF) composite was developed for the sensitive and selective detection of nimesulide, a widely used nonsteroidal anti-inflammatory drug. The $MnMoO_4$ nanoparticles were synthesized via a deep eutectic solvent-assisted hydrothermal route and subsequently integrated onto acid-functionalized carbon nanofibers (CNFs) to form a hybrid electrocatalyst with enhanced conductivity and active surface area. Comprehensive physicochemical characterization using X-ray diffraction (XRD), Fourier transform infrared (FTIR), Raman spectroscopy, X-ray photoelectron spectroscopy (XPS), field emission scanning electron microscopy (FESEM), transmission electron microscopy (TEM), and selected area electron diffraction (SAED) confirmed the successful formation of highly crystalline $MnMoO_4$ with uniform dispersion on the CNF matrix. Electrochemical investigations revealed that the $MnMoO_4$/CNF-modified glassy carbon electrode exhibited outstanding redox activity toward nimesulide, achieving a wide linear detection range of 0.00125−3525.25 μM, a low limit of detection of 0.0026 μM, high sensitivity 1.27 $\mu A\ \mu M^{-1}\ cm^2$, and a high correlation coefficient (R^2 = 0.982). The sensor demonstrated favorable surface-controlled electrochemical kinetics, excellent stability over extended operation (1600 s), and high selectivity against common interfering substances such as phenols, uric acid, and glucose. Notably, the sensor exhibited remarkable reproducibility (RSD 98.3%) across independently fabricated electrodes. Real sample analyses in spiked blood plasma and pharmaceutical tablet extracts yielded satisfactory recoveries, validating the sensor's matrix compatibility and analytical robustness. The synergistic integration of electroactive $MnMoO_4$ and conductive CNF enables efficient electron transfer, high electrocatalytic activity, and structural stability, positioning the $MnMoO_4$/CNF composite as a promising candidate for practical applications in therapeutic drug monitoring and pharmaceutical quality assurance.

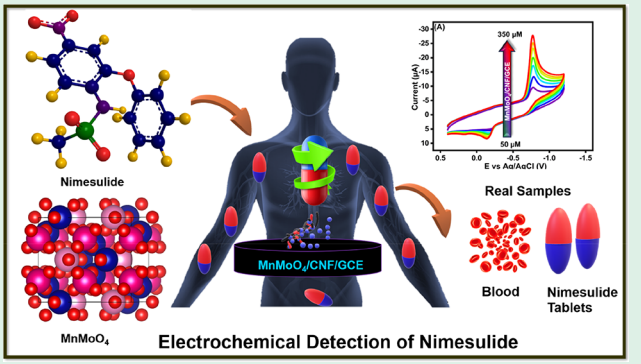

KEYWORDS: *nimesulide, electrochemical sensor, nonsteroidal anti-inflammatory drug, drug monitoring, deep-eutectic solvent*

1. INTRODUCTION

The widespread contamination of aquatic environments with pharmaceutical residues has become an escalating global issue, presenting serious threats to both ecological integrity and human health. The continual rise in pharmaceutical consumption worldwide has led to the excretion of considerable amounts of unmetabolized compounds, which are subsequently introduced into wastewater systems through domestic and hospital effluents.[1−3] Conventional wastewater treatment plants are often inadequate in fully eliminating these micropollutants, leading to their persistence in surface and groundwater at trace concentrations.[4] Among various pharmaceutical contaminants, nimesulide, a commonly prescribed nonsteroidal anti-inflammatory drug (NSAID), is frequently detected in aquatic environments owing to its high physicochemical stability and limited susceptibility to microbial degradation. Its persistent nature facilitates prolonged environmental presence, and chronic exposure has been shown to induce cytotoxicity and hepatotoxicity in aquatic biota. Furthermore, its tendency to bioaccumulate within trophic levels raises substantial concerns regarding its potential to disrupt aquatic ecosystems and pose long-term risks to human health through biomagnification.[5−7] In light of

Received: May 30, 2025
Revised: September 2, 2025
Accepted: September 7, 2025
Published: September 11, 2025

https://doi.org/10.1021/acsabm.5c01031
ACS Appl. Bio Mater. 2025, 8, 8864−8879

Scheme 1. Schematic Illustration of the Synthesis of $MnMoO_4$ Nanoparticles, Functionalization of CNF, and Preparation of the $MnMoO_4$@f-CNF Nanocomposite

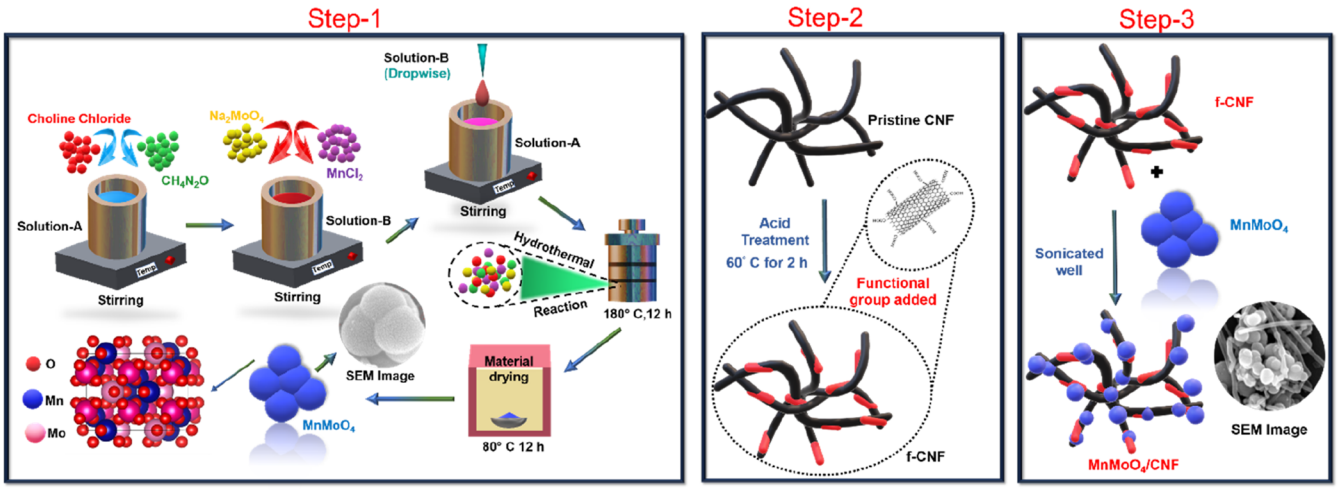

increasing regulatory and scientific attention on pharmaceutical pollutants, the development of rapid, sensitive, and selective analytical techniques for the real-time monitoring of drugs such as nimesulide is of critical importance. Conventional analytical methods, including high-performance liquid chromatography (HPLC), gas chromatography–mass spectrometry (GC–MS), and ultraviolet–visible (UV–vis) spectrophotometry, offer high accuracy and sensitivity. However, these techniques are often limited by their high cost, labor-intensive procedures, requirement for skilled personnel, and the need for extensive sample pretreatment.[8−10] These drawbacks hinder their applicability for routine and on-site monitoring, particularly in resource-limited settings. In contrast, electrochemical sensing technologies have garnered increasing interest due to their low cost, operational simplicity, portability, rapid response, and potential for miniaturization.[11,12] The performance of electrochemical sensors, however, is fundamentally governed by the properties of the electrode materials employed. Achieving high sensitivity, selectivity, and stability in trace-level detection requires functional electrode materials that possess a high surface area, rapid electron transfer capabilities, and abundant active sites for analyte interaction.[13−16]

In this context, manganese molybdate ($MnMoO_4$) has attracted considerable interest owing to its favorable electrochemical characteristics, including multivalent redox centers, rapid redox kinetics, and structural robustness.[17−19] The synergistic redox behaviors of Mn^{2+}/Mn^{3+} and Mo^{6+}/Mo^{4+} facilitates enhanced electrocatalytic activity, rendering $MnMoO_4$ a promising candidate for electrochemical applications.[20,21] Nevertheless, the practical deployment of pristine $MnMoO_4$ is constrained by its inherently low electrical conductivity and propensity for particle agglomeration, which limits the effective exposure of electroactive sites.[22] To overcome these limitations, a composite engineering strategy was adopted, involving the integration of $MnMoO_4$ with carbon nanofibers (CNFs). CNFs exhibit excellent electrical conductivity, chemical stability, and a high aspect ratio, making them ideal scaffolds for supporting and dispersing metal oxide nanoparticles.[23−26] The resulting $MnMoO_4$/CNF hybrid architecture effectively suppresses particle agglomeration, enhances charge transport, and facilitates efficient ion–electron exchange at the electrode–electrolyte interface.[22,27,28] Furthermore, the interconnected conductive network provided by CNFs improves the accessibility of redox-active sites, increases the effective surface area, and enhances the mechanical integrity of the composite, thereby significantly elevating sensor performance.[29−31] Venkatesh et al. synthesized a $MnMoO_4$/graphene nanosheet hybrid via a low-power sonochemical method.[32] However, the resulting $MnMoO_4$ crystallites were primarily microscale, which may limit electroactive surface area and impede charge transport. In the present study, a deep eutectic solvent-assisted hydrothermal approach was adopted to synthesize nanoscale $MnMoO_4$ with uniform dispersion and high crystallinity. The deep eutectic solvent (DES) medium facilitates controlled nucleation without surfactants, yielding finer particles with greater surface exposure. Coupling these nanostructures with functionalized carbon nanofibers produced a $MnMoO_4$/CNF composite with improved conductivity, higher surface area, and more efficient electron transfer, offering clear advantages in electrochemical material performance. Importantly, the electrochemical interface constructed using $MnMoO_4$/CNF exhibits strong physicochemical interactions with electroactive pharmaceutical molecules such as nimesulide, facilitating their detection through adsorption and redox-based mechanisms. This synergistic integration of $MnMoO_4$'s redox functionality with the conductive matrix of CNFs enables the construction of a high-performance sensing platform specifically tailored for pharmaceutical pollutant detection.

In the present study, we report the design, fabrication, and electrochemical characterization of a $MnMoO_4$/CNF-modified glassy carbon electrode (GCE) for the sensitive and selective detection of nimesulide. The sensor exhibited outstanding electrocatalytic behaviors, attributed to the effective coupling between $MnMoO_4$'s redox-active centers and CNF's conductive framework. The fabricated sensor achieved a low limit of detection of 0.0026 μM, and high sensitivity of 1.27 $\mu A\,\mu M^{-1}$ cm^2, along with excellent selectivity against commonly coexisting interferents. Its practical utility was demonstrated through successful application in the analysis of human blood serum samples and commercial nimesulide tablet formulations, requiring minimal sample preparation. Recovery studies further validated the sensor's accuracy and robustness

https://doi.org/10.1021/acsabm.5c01031
ACS Appl. Bio Mater. 2025, 8, 8864−8879

Scheme 2. Illustration of the GCE Cleaning and Modification Steps Using $MnMoO_4$, f-CNF, and $MnMoO_4$@f-CNF for Electrochemical Sensing of Nimesulide

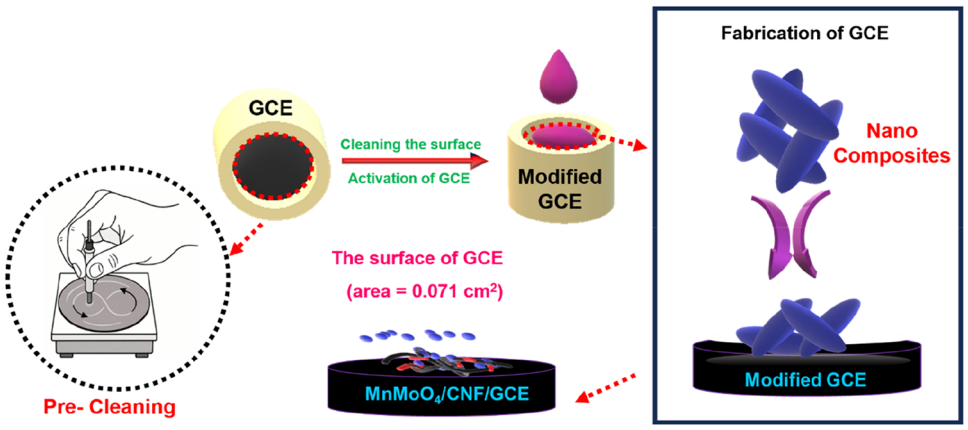

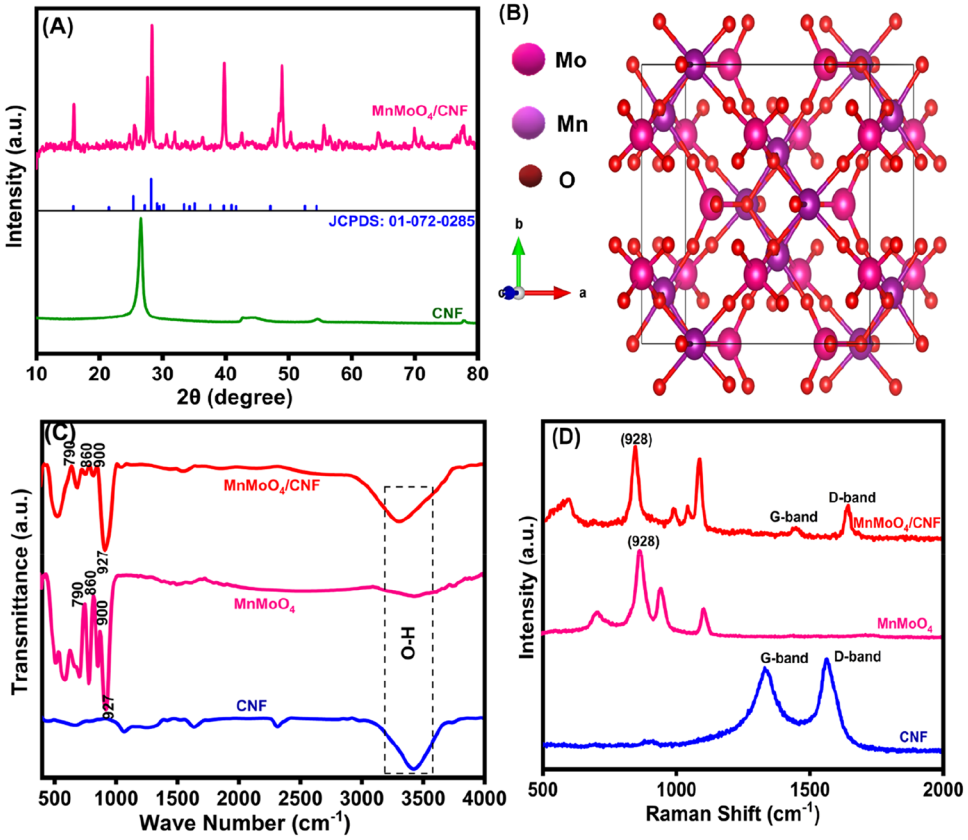

Figure 1. (A) XRD patterns of CNF, $MnMoO_4$, and $MnMoO_4$/CNF, (B) Crystal structure of $MnMoO_4$, (C) FTIR data of CNF, $MnMoO_4$, and $MnMoO_4$/CNF, (D) Raman Spectra of CNF, $MnMoO_4$, and $MnMoO_4$/CNF.

in complex biological matrices, confirming its potential in clinical diagnostics and pharmaceutical quality control.

2. CHEMICALS AND METHODS

All chemicals used in this study were obtained from Sigma-Aldrich in analytical grade and were utilized without further purification. Detailed information on the specific chemicals, buffer solution preparation, and instrumentation used can be found in S1.

2.1. Synthesis of $MnMoO_4$ Nanoparticles. $MnMoO_4$ nanoparticles were synthesized via a deep eutectic solvent (DES)-assisted hydrothermal method, as illustrated in Scheme 1. In a typical procedure, solution A was prepared by dissolving urea (CH_4N_2O, 5.58 g) and choline chloride (4.80 g) in deionized water at a molar ratio of 2:1. The mixture was stirred continuously for 1 h at room temperature to form a homogeneous deep eutectic solvent. This DES played a dual role as both a green solvent and a structure-directing agent, providing a tunable reaction medium that enhanced nucleation and particle dispersion.

In parallel, solution B was formulated by dissolving manganese(II) chloride ($MnCl_2$, 0.5 g) and sodium molybdate (Na_2MoO_4, 0.5 g) in deionized water. The metal precursor solution (B) was then introduced dropwise into the DES (solution A) under constant magnetic stirring for 30 min to ensure uniform mixing and to initiate the coordination of Mn^{2+} and MoO_4^{2-} ions within the DES matrix. The resulting transparent pink mixture was transferred into a 100 mL Teflon-lined stainless-steel autoclave and subjected to hydrothermal treatment at 180 °C for 12 h. This high-temperature and pressure

https://doi.org/10.1021/acsabm.5c01031
ACS Appl. Bio Mater. 2025, 8, 8864−8879

condition facilitated the formation of $MnMoO_4$ nanoparticles through controlled crystallization and growth. Upon completion, the autoclave was cooled to room temperature naturally. The precipitate was collected by centrifugation, washed several times with ethanol and deionized water to remove any unreacted species and residual DES, and subsequently dried at 80 °C for 24 h in a hot air oven. The resulting $MnMoO_4$ exhibited a well-defined morphology and phase purity suitable for further composite fabrication.[33]

2.2. Functionalization of Carbon Nanofibers (CNF). Pristine CNFs were subjected to acid treatment to introduce oxygen-containing functional groups on their surface. Specifically, the CNFs were refluxed in a mixed acid solution of concentrated HNO_3 and H_2SO_4 (1:3 v/v) at 60 °C for 2 h. This oxidative treatment facilitated the incorporation of carboxyl, hydroxyl, and carbonyl groups, thereby improving dispersibility and enhancing surface reactivity. After treatment, the functionalized CNFs (f-CNFs) were thoroughly washed with deionized water until a neutral pH was achieved and then dried at ambient temperature.[34,35]

2.3. Preparation of $MnMoO_4$@f-CNF Electrocatalyst. The $MnMoO_4$@f-CNF electrocatalyst was prepared by a facile ultrasonication-assisted method. In a typical procedure, the as-synthesized $MnMoO_4$ nanoparticles were dispersed in deionized water along with f-CNFs in a suitable weight ratio. The mixture was ultrasonicated for 30 min to ensure uniform dispersion and strong interaction between $MnMoO_4$ and the functional groups on the CNF surface. The resulting hybrid material, $MnMoO_4$@f-CNF, exhibited a well-interconnected architecture, as confirmed by SEM analysis, indicating successful integration of $MnMoO_4$ nanoparticles onto the f-CNF framework.

2.4. Electrode Fabrication. Before modifying the GCE with the electrocatalysts $MnMoO_4$ nanoparticles, f-CNF, and $MnMoO_4$@f-CNF nanocomposite, it was essential to thoroughly clean the electrode surface. This step, illustrated in Scheme 2, ensures the removal of surface contaminants, such as organic residues, metal oxides, or other adsorbed species, which could hinder the electrode's performance. The GCE was polished using alumina slurry (0.05 μm) to create a smooth, well-defined surface. Proper cleaning is crucial as it eliminates resistive effects, maximizes active site exposure, and facilitates efficient electron transfer during electrochemical reactions. Additionally, it minimizes nonspecific adsorption, enhancing the interaction between the electrode and the electrocatalysts, thereby improving the electrochemical performance and reproducibility of the sensor.[36,37]

After polishing, the GCE was rinsed with DI·H_2O and dried under nitrogen. A 2 mg aliquot of each electrocatalyst $MnMoO_4$ nanoparticles, f-CNF, and $MnMoO_4$@f-CNF was dispersed in 3 mL of DI·H_2O and sonicated for 30 min to ensure a uniform distribution. Then, 6 μL of the solution was drop-cast onto the surface of the GCE. The modified electrodes $MnMoO_4$/GCE, f-CNF/GCE, and $MnMoO_4$@f-CNF/GCE were dried at 60 °C and subsequently used for electrochemical analysis. The electrochemical detection of nimesulide was performed within the potential window of 0.5 to −1.4 V (vs Ag/AgCl) using a conventional three-electrode system.[38]

3. RESULTS AND DISCUSSION

3.1. XRD Analysis. The phase composition and crystallinity of the synthesized samples were examined using X-ray diffraction, as shown in Figure 1A. The pristine carbon nanofibers (CNF) display a broad diffraction peak centered at approximately $2\theta \approx 26°$, which corresponds to the (002) plane of graphitic carbon. This broad peak signifies a partially disordered or amorphous carbon structure with turbostratic stacking, a common feature in acid-treated CNFs. In contrast, the $MnMoO_4$ sample exhibits sharp and well-defined diffraction peaks, indicating a highly crystalline nature. These peaks are in excellent agreement with the standard diffraction pattern of orthorhombic $MnMoO_4$ (JCPDS Card No. 01−072−0285), with prominent reflections observed at 2θ values corresponding to the (111), (200), (220), (400), and (511) planes. This confirms the successful synthesis of phase-pure $MnMoO_4$ via the DES-assisted hydrothermal route. The $MnMoO_4$/CNF composite retains all the major diffraction features of $MnMoO_4$, indicating that the crystallographic structure of the metal molybdate remains intact upon composite formation. Additionally, the characteristic broad peak of CNF persists, although with reduced intensity due to partial coverage by $MnMoO_4$ nanoparticles. The coexistence of peaks from both components affirms the successful integration of $MnMoO_4$ into the CNF matrix without inducing phase transformation or degradation.[33]

3.2. Crystal Structure of $MnMoO_4$. The crystal structure of $MnMoO_4$ is illustrated in Figure 1B, which shows the orthorhombic unit cell composed of interconnected MnO_6 and MoO_6 octahedra. In this framework, Mn^{2+} and Mo^{6+} cations are coordinated by oxygen atoms, forming distorted octahedral geometries that are linked through corner-sharing O atoms. This configuration results in a robust three-dimensional framework that supports ionic mobility and structural stability. Such features are particularly advantageous for electrochemical applications, where high crystallinity, defect-tolerance, and open-framework architectures are desirable for enhanced charge transport and active surface area.

3.3. FT-IR Spectroscopy. Fourier-transform infrared (FT-IR) spectroscopy was employed to investigate the chemical bonding and surface functionalities of the individual and composite materials, as depicted in Figure 1C. The CNF spectrum displays a broad absorption band centered near 3420 cm^{-1}, corresponding to the stretching vibrations of hydroxyl (−OH) groups. This feature arises due to the introduction of oxygen-containing functional groups during acid oxidation, which enhances the hydrophilicity and dispersion stability of CNFs. In the case of $MnMoO_4$, multiple strong bands are observed in the 500−900 cm^{-1} region, specifically at 580, 680, and 790 cm^{-1}. These are assigned to the stretching vibrations of metal−oxygen bonds, with the bands around 580 and 680 cm^{-1} attributed to Mn−O stretching modes and the band near 790 cm^{-1} corresponding to Mo−O vibrations in MoO_6 octahedra. For the $MnMoO_4$/CNF composite, the FTIR spectrum shows characteristic peaks from both components. The presence of metal−oxygen vibrations confirm the successful formation of $MnMoO_4$, while the persistence of the O−H stretching band and other oxygen-functionalized peaks confirms that the CNF surface remains functionalized after composite formation. This indicates a good interaction between the two components, likely through hydrogen bonding and electrostatic interactions, which may facilitate electron transfer in electrocatalytic applications.[33]

3.4. Raman Spectroscopy. Raman spectroscopy was further conducted to probe the structural characteristics and interactions between $MnMoO_4$ and CNF, as illustrated in Figure 1D. The pristine CNF displays two characteristic Raman bands: the D-band at ∼1340 cm^{-1}, representing the breathing modes of sp^3-hybridized carbon atoms due to structural defects or disorder, and the G-band at ∼1580 cm^{-1}, which corresponds to the E_{2g} mode of sp^2-hybridized carbon domains. The intensity ratio (I_D/I_G) serves as an indicator of graphitization and defect density, which is crucial for electron conductivity in sensing applications. $MnMoO_4$ exhibits a dominant vibrational band at ∼928 cm^{-1}, attributed to the symmetric stretching vibrations of Mo−O bonds in MoO_6 octahedra, consistent with literature reports for crystalline

https://doi.org/10.1021/acsabm.5c01031
ACS Appl. Bio Mater. 2025, 8, 8864−8879

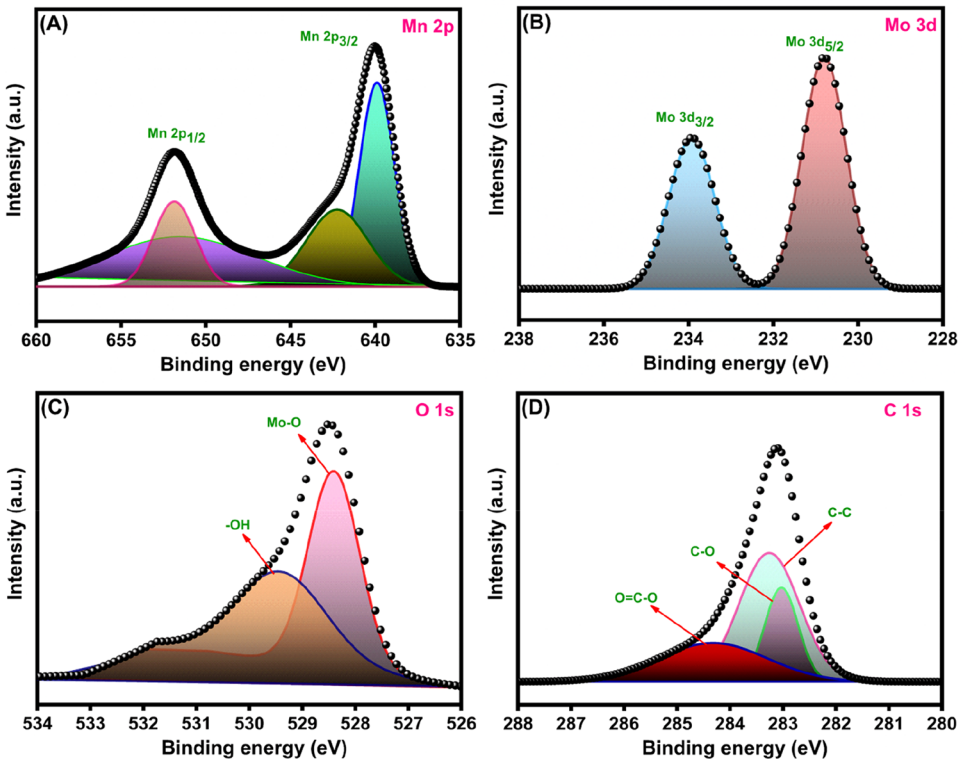

Figure 2. XPS spectra of the $MnMoO_4$/CNF composite, with (A) high-resolution Mn 2p, (B) high-resolution Mo 3d, (C) high-resolution O 1s, and (D) high-resolution C 1s spectra.

molybdates. This peak is a vibrational fingerprint confirming the structural integrity of $MnMoO_4$. The $MnMoO_4$/CNF composite spectrum retains both the carbon-related D and G bands as well as the Mo−O characteristic band. The presence of all these features in a single spectrum confirms the successful hybridization of $MnMoO_4$ nanoparticles onto the CNF surface.[39] Notably, subtle shifts and intensity changes in the Raman bands suggest strong interfacial interactions between $MnMoO_4$ and functional groups on CNF, which can lead to improved charge transfer efficiency in electrochemical systems.

3.5. XPS Analysis. X-ray photoelectron spectroscopy (XPS) was employed to investigate the elemental composition, oxidation states, and surface functionalities of the $MnMoO_4$/CNF composite. The high-resolution spectra of Mn 2p, Mo 3d, O 1s, and C 1s are depicted in Figure 2A−D. As shown in Figure 2A, the Mn 2p spectrum exhibits two distinct peaks located at binding energies of approximately 641.6 and 653.3 eV, corresponding to Mn $2p_{3/2}$ and Mn $2p_{1/2}$, respectively. These peaks are characteristic of Mn^{2+} oxidation state in $MnMoO_4$. The spin−orbit splitting of ∼11.7 eV between these peaks further confirms the presence of Mn in a divalent state. Deconvolution of the Mn $2p_{3/2}$ peak reveals minor contributions from Mn^{3+} species, suggesting a mixed-valence state which may be beneficial for redox-related electrochemical processes due to enhanced charge transport. The Mo 3d core level spectrum (Figure 2B) shows two well-resolved peaks centered at binding energies of 231.5 and 234.6 eV, assigned to Mo $3d_{5/2}$ and Mo $3d_{3/2}$, respectively. These peaks are indicative of Mo^{6+} oxidation state, in agreement with previous reports for molybdate-based compounds. The energy separation of ∼3.1 eV between the two spin−orbit components support the presence of a high-valent molybdenum environment, confirming the formation of MoO_6 octahedra in the composite.

The O 1s spectrum, shown in Figure 2C, reveals two major peaks located at ∼528.8 and ∼530.3 eV. The peak at 528.8 eV corresponds to lattice oxygen (Mo−O and Mn−O bonds), indicating the presence of metal−oxygen bonding within the $MnMoO_4$ framework. The higher binding energy component at 530.3 eV is attributed to surface −OH groups and adsorbed oxygen species, typically associated with defect sites or functionalized CNF surfaces. The presence of hydroxyl groups suggests improved hydrophilicity and potential active sites for electrochemical reactions. The high-resolution C 1s spectrum[40] (Figure 2D) provides insights into the surface chemistry of the carbon nanofiber matrix. The spectrum can be deconvoluted into three distinct components: the primary peak at 284.6 eV corresponding to sp^2-hybridized graphitic carbon (C−C), a secondary peak at 286.1 eV attributed to C−O bonds, and a minor peak at 288.5 eV associated with carboxylate or carbonyl groups (O═C−O). These oxygenated carbon species confirm the successful functionalization of CNFs, which facilitates strong interactions with $MnMoO_4$ nanoparticles and promotes interfacial electron transfer. The overall spectrum is provided in Supporting Information (Figure S1). Collectively, the XPS data validate the successful synthesis of $MnMoO_4$/CNF with appropriate oxidation states of Mn and Mo, the presence of surface oxygen functionalities, and the incorporation of functionalized carbon species. These features synergistically contribute to the electrocatalytic potential of the composite material.

3.6. Morphological and Elemental Mapping Analysis. The surface morphology and microstructural characteristics of CNF, $MnMoO_4$, and the $MnMoO_4$/CNF composite were studied using field-emission scanning electron microscopy

https://doi.org/10.1021/acsabm.5c01031
ACS Appl. Bio Mater. 2025, 8, 8864−8879

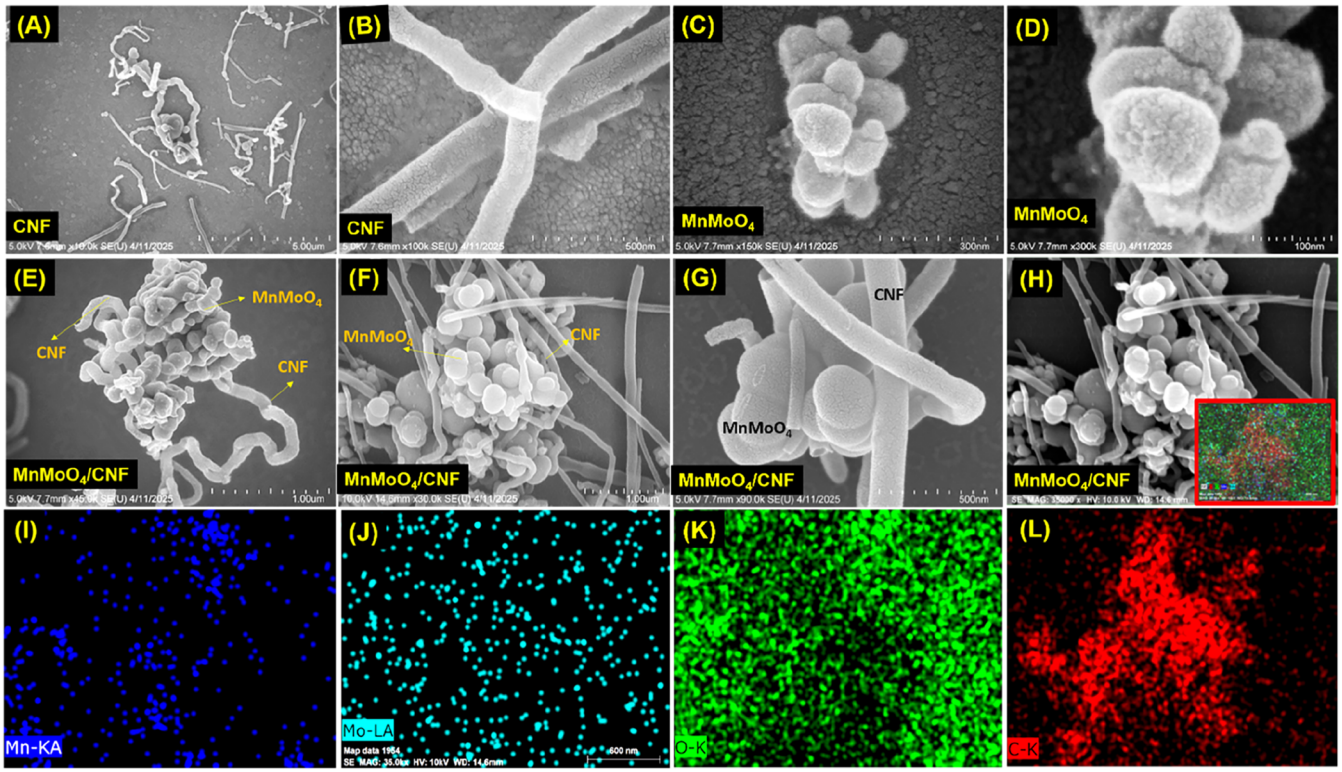

Figure 3. (A, B) FESEM images of CNF, (C, D) $MnMoO_4$ at different scales, (E–G) $MnMoO_4$/CNF composite; elemental mappings: (H) Mixed elements within the composite, (I) distribution of Mn, (J) distribution of Mo, (K) distribution of O, and (L) distribution of C.

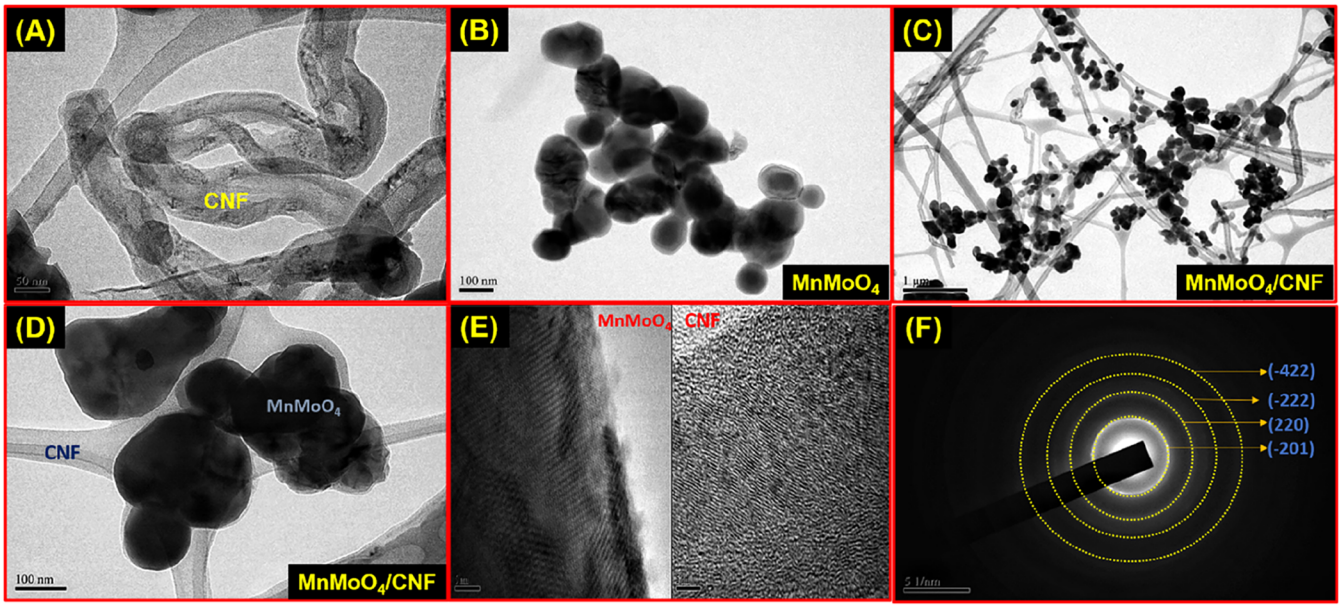

Figure 4. (A) TEM images of CNF, (B) $MnMoO_4$, (C–D) $MnMoO_4$ /CNF composite, (E) HR-TEM images showing the $MnMoO_4$ and CNF, (F) SAED pattern of $MnMoO_4$ /CNF composite.

(FESEM), and the results are presented in Figure 3A–H. Additionally, energy-dispersive X-ray spectroscopy (EDS) elemental mapping was conducted to confirm the spatial distribution of constituent elements within the composite.

3.6.1. FESEM Morphology of CNF and $MnMoO_4$. The FESEM images of the pristine carbon nanofibers are shown in Figure 3A,B. The CNFs display a long, entangled, and smooth fibrous morphology with uniform diameters in the submicron range.[41] The absence of agglomeration and the fibrous network indicate good dispersion and high surface area, which is advantageous for serving as a conductive scaffold in composite materials. The morphology of pure $MnMoO_4$ nanoparticles is presented in Figure 3C,D at increasing magnifications. The $MnMoO_4$ exhibits a hierarchical structure composed of aggregated nanosheets or petal-like entities forming spherical architectures. This three-dimensional morphology is known to offer a high specific surface area and interconnected porosity, facilitating enhanced electrochemical activity due to abundant

https://doi.org/10.1021/acsabm.5c01031
ACS Appl. Bio Mater. 2025, 8, 8864–8879

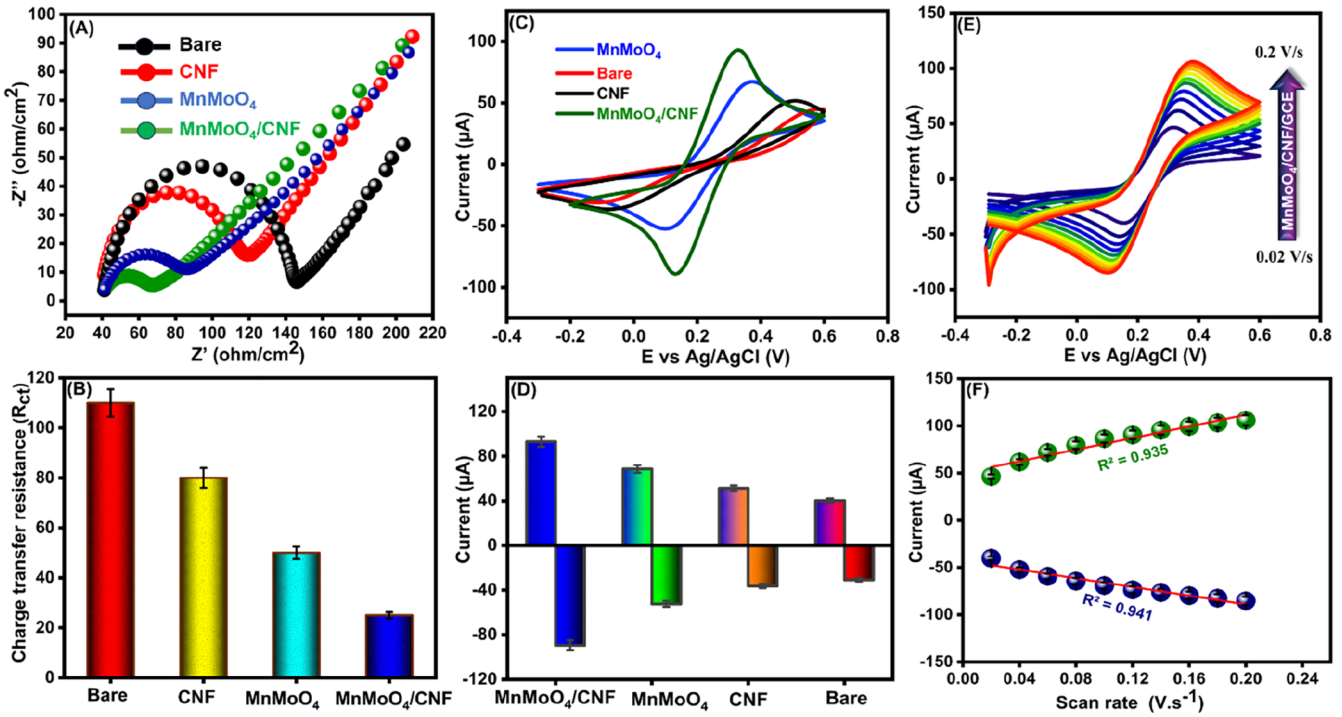

Figure 5. (A) EIS spectra of bare GCE, CNF/GCE, $MnMoO_4$/GCE, and $MnMoO_4$/CNF/GCE in 5 mM FCN and 0.1 M KCl. (B) Graph of EIS results from (A). (C) CV profiles of bare GCE, CNF, $MnMoO_4$, and $MnMoO_4$/CNF in 5 mM FCN under 0.1 M KCl. (D) Plot of CV results from (C). (E) Scan rate studies for $MnMoO_4$/CNF/GCE composite ranging from 0.02 to 0.2 V s^{-1}. (F) Linear relationship of current vs scan rate for $MnMoO_4$/CNF/GCE.

active sites and better electrolyte accessibility.[42] The FESEM EDAX analysis is provided in Figure S2.

3.6.2. Morphology of $MnMoO_4$/CNF Composite. The FESEM images of the $MnMoO_4$/CNF composite are shown in Figure 3E−G. The $MnMoO_4$ nanostructures are observed to be uniformly anchored onto the surface of the CNF matrix. The spherical aggregates of $MnMoO_4$ intimately interact with the CNF framework, which provides a highly conductive and mechanically stable platform for the metal oxide. This hybrid morphology ensures effective electron transport and structural integrity during electrochemical processes. The high magnification images confirm tight interfacial contact between the components, supporting strong interfacial synergy essential for sensor or catalytic performance. The low-magnification composite image in Figure 3H further confirms the homogeneity of the $MnMoO_4$ dispersion over the CNF surface. The inset shows the corresponding EDS elemental mapping area, providing a visual overview of the composite's elemental distribution.

3.6.3. Elemental Mapping. To verify the elemental composition and distribution of the $MnMoO_4$/CNF hybrid, EDS elemental mapping was performed, as shown in Figure 3I−L. The mapping results reveal the uniform distribution of manganese (Mn) (Figure 3I), molybdenum (Mo) (Figure 3J), and oxygen (O) (Figure 3K) throughout the CNF network. Carbon (C), originating from the CNF substrate, is distributed uniformly as well (Figure 3L). The colocalization of Mn, Mo, O, and C confirms the successful integration of $MnMoO_4$ nanoparticles onto the functionalized CNF surface without phase segregation or clustering. This elemental homogeneity is critical for ensuring consistent electrochemical behavior across the electrode surface and further substantiates the effectiveness of the synthesis strategy employed. The FESEM-EDX elemental mapping results provide supporting evidence for the material composition and elemental distributions, as shown in Figure S2, further validating the successful formation of the synthesized nanocomposite.

3.7. TEM and SAED. Transmission electron microscopy (TEM) and high-resolution TEM (HR-TEM) analyses were carried out to further investigate the microstructure, morphology, and crystallinity of the CNF, $MnMoO_4$, and the $MnMoO_4$/CNF composite. The corresponding images are provided in Figure 4A−F.

3.7.1. TEM Morphology of CNF and $MnMoO_4$. As shown in Figure 4A, the CNFs exhibit a smooth, tubular, and entangled structure with diameters in the range of tens of nanometers. The hollow or partially collapsed tubular morphology is typical of acid-treated CNFs and is beneficial for anchoring nanoparticles due to the high surface area and functionalized surface. The TEM image of $MnMoO_4$ nanoparticles in Figure 4B reveals aggregated spherical structures with relatively uniform size distribution. These nanospheres are composed of densely packed nanocrystallites that contribute to their high surface energy. Such morphology is known to provide numerous exposed active sites, advantageous for catalytic and sensing applications.

3.7.2. TEM of $MnMoO_4$/CNF Composite. Figure 4C,D illustrates the morphology of the $MnMoO_4$/CNF hybrid composite. The $MnMoO_4$ nanospheres are clearly seen anchored onto the surface of the carbon nanofibers, forming an interconnected hybrid network. This intimate contact is crucial for ensuring efficient electron transfer across the interface and minimizing interfacial resistance. The composite structure demonstrates that the CNFs serve as a flexible and conductive support, while the $MnMoO_4$ nanoparticles provide electrocatalytically active sites. In Figure 4D, the contrast

https://doi.org/10.1021/acsabm.5c01031
ACS Appl. Bio Mater. 2025, 8, 8864−8879

Scheme 3. Possible Electrochemical Mechanism of Nimesulide

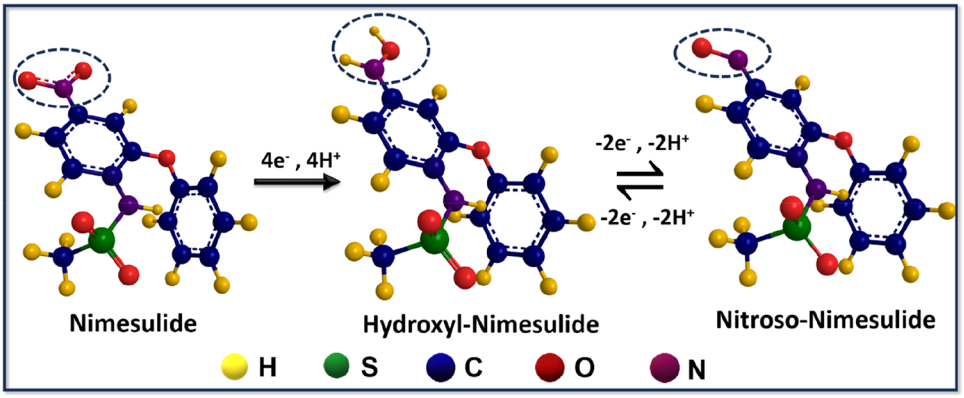

between the dense $MnMoO_4$ particles and the lighter CNF matrix further confirms strong interfacial coupling between the two phases. This hybrid architecture is expected to enhance both mechanical integrity and electrochemical performance by combining the advantages of both components.

3.7.3. High-Resolution TEM and Interface Analysis. The high-resolution TEM image in Figure 4E provides atomic-level insights into the interface between $MnMoO_4$ and CNF. Clear lattice fringes can be observed in the $MnMoO_4$ region, indicative of its high crystallinity. The measured interplanar spacing corresponds well to the (220) lattice plane of orthorhombic $MnMoO_4$. The adjacent CNF region displays a less ordered, graphitic lattice structure with short-range order, confirming the presence of amorphous or turbostratic carbon. The coherent interface between $MnMoO_4$ and CNF suggests good electronic coupling, which is beneficial for rapid charge transfer processes during electrochemical operation.

3.7.4. SAED Pattern. The selected area electron diffraction (SAED) pattern of the $MnMoO_4$/CNF composite is displayed in Figure 4F. The diffraction rings correspond to the $(\bar{2}01)$, (220), $(\bar{2}22)$, and $(\bar{4}22)$ planes of $MnMoO_4$, which are in good agreement with the XRD results. The presence of sharp and continuous rings indicates the polycrystalline nature of the $MnMoO_4$ nanoparticles. The absence of diffraction spots from CNF is consistent with its low crystallinity, further supporting the conclusion that CNF mainly serves as a conductive and porous scaffold. Together, the TEM and SAED analyses confirm the successful integration of crystalline $MnMoO_4$ onto functionalized CNFs, forming a robust and well-connected hybrid architecture suitable for electrochemical sensing applications. The TEM images combined with elemental mapping shown in Figure S3 further support the successful synthesis of the nanocomposite, revealing its internal morphology and confirming the homogeneous distribution of constituent elements.

3.8. Electrochemical Characterization. To evaluate the interfacial electron transfer kinetics and electroactive behavior of the fabricated electrodes, electrochemical impedance spectroscopy (EIS) and cyclic voltammetry (CV) studies were carried out using a standard redox probe of 5 mM $[Fe(CN)_6]^{3-/4-}$ in 0.1 M KCl. Comparative analysis was conducted on bare glassy carbon electrode (GCE), CNF-modified GCE (CNF/GCE), $MnMoO_4$-modified GCE ($MnMoO_4$/GCE), and $MnMoO_4$/CNF composite-modified GCE ($MnMoO_4$/CNF/GCE). The corresponding data are shown in Figure 5A–F.

3.8.1. EIS Analysis. Nyquist plots, as shown in Figure 5A, illustrate the impedance characteristics of the four electrode systems. The semicircle portion observed in the high-frequency region represents the charge transfer resistance (R_{cpplt}), which is a critical parameter reflecting the ease of electron exchange at the electrode–electrolyte interface. The bare GCE exhibited a large semicircle with a high R_{ct} value of approximately bare 114 Ω, indicating sluggish charge transfer behavior due to the absence of any conductive or catalytic material on the electrode surface. In contrast, the CNF/GCE displayed a considerably smaller semicircle, with an R_{ct} of CNF 80 Ω, which can be attributed to the high electrical conductivity, large surface area, and interconnected network of the carbon nanofibers that facilitate charge transport. The $MnMoO_4$/GCE exhibited a further reduction in R_{ct} to $MnMoO_4$ 47 Ω, highlighting the redox-active nature and electrochemical responsiveness of $MnMoO_4$ nanoparticles. Significantly, the $MnMoO_4$/CNF/GCE electrode demonstrated the lowest R_{ct} value of only $MnMoO_4$/CNF 26 Ω, indicating superior interfacial electron transfer kinetics due to the synergistic combination of highly conductive CNF and electroactive $MnMoO_4$. These comparative results are quantitatively represented in Figure 5B, underscoring the enhanced conductivity and catalytic properties imparted by the composite architecture.

3.8.2. CV Analysis. CV studies were performed to investigate the electrochemical redox behavior of the modified and unmodified electrodes, and the voltammograms are displayed in Figure 5C. The bare GCE showed a low redox current response of bare 125 μA and a large peak-to-peak separation (ΔE_p) of bare 850 mV, indicating limited electrochemical activity and high resistance to charge transfer. Upon modification with CNF, the redox peak currents increased to CNF 145 μA and ΔE_p decreased to CNF 710 mV, reflecting improved electron transfer and surface reactivity due to the enhanced conductive properties of CNF. For $MnMoO_4$/GCE, the redox response further improved, with peak currents of $MnMoO_4$ 190 μA and ΔE_p to $MnMoO_4$ 660 mV, owing to the pseudocapacitive nature and redox activity of the metal molybdate structure. The $MnMoO_4$/CNF/GCE composite electrode exhibited the most pronounced redox response, with peak currents reaching $MnMoO_4$/CNF 225 μA and the smallest ΔE_p of $MnMoO_4$/CNF 610 mV, indicative of rapid electron transfer, minimal internal resistance, and abundant accessible active sites. These results are summarized in Figure 5D and validate the beneficial role of the $MnMoO_4$–CNF hybrid architecture in promoting electrochemical activity.

https://doi.org/10.1021/acsabm.5c01031
ACS Appl. Bio Mater. 2025, 8, 8864–8879

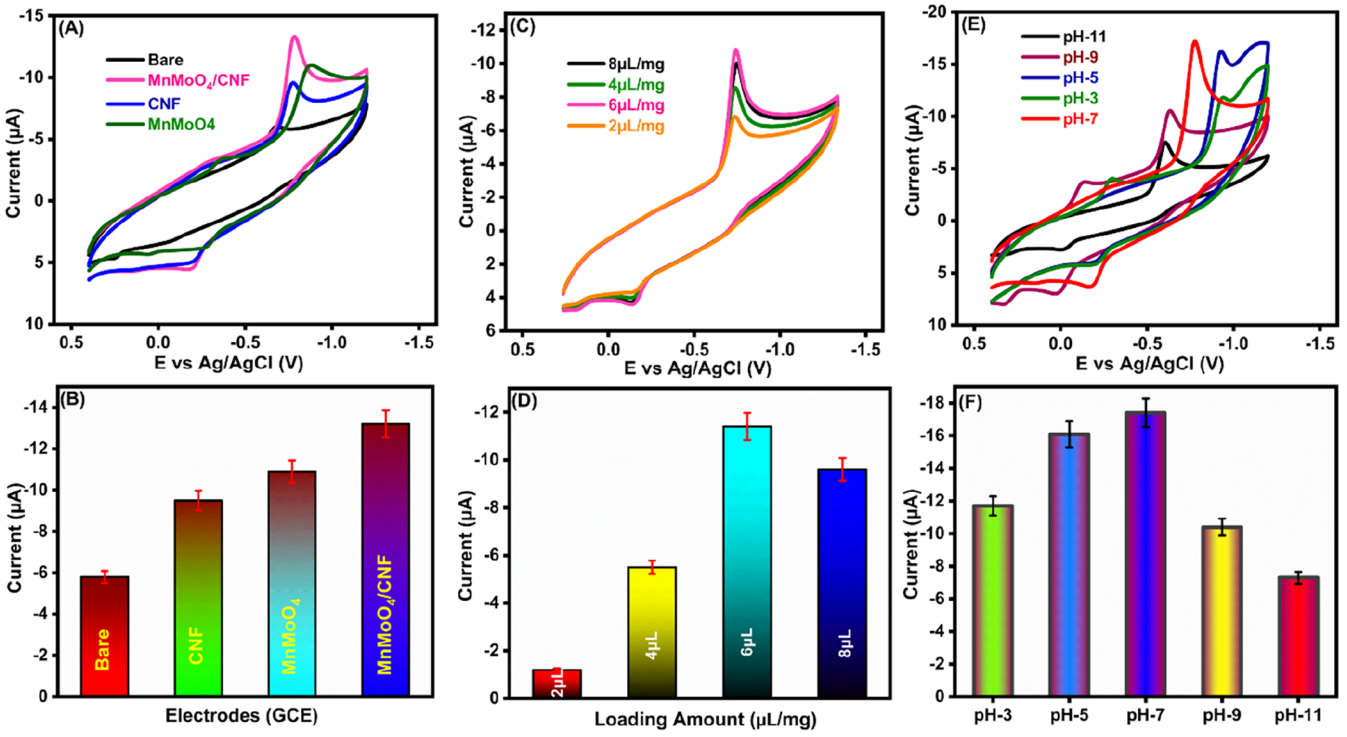

Figure 6. (A) CV profiles for bare GCE, CNF/GCE, $MnMoO_4$/GCE, and $MnMoO_4$/CNF/GCE in 100 μM nimesulide solution. (B) Plot showing CV current responses for each electrode modification. (C) CV responses of $MnMoO_4$/CNF/GCE with varying loading amounts of the composite. (D) Calibration plot derived from (C), illustrating the effect of composite loading on sensor performance. (E) CV behavior of $MnMoO_4$/CNF/GCE across pH values 3 to 11 in nimesulide. (F) Graph plotting pH against current response.

3.8.3. Scan Rate Studies. To understand the kinetics of the redox process at the $MnMoO_4$/CNF/GCE interface, CV measurements were performed at varying scan rates ranging from 0.02 to 0.2 V s^{-1} Figure 5E. With increasing scan rate, both anodic and cathodic peak currents increased proportionally, and the voltammograms retained their quasi-reversible shape, suggesting surface-confined electrochemical behavior. The linear relationships between peak current and scan rate are depicted in Figure 5F, with calculated correlation coefficients (R^2) of = 0.935 for the anodic peak and (R^2) of = 0.941 for the cathodic peak. These high R^2 values confirm that the redox process is governed by adsorption-controlled kinetics rather than diffusion-limited behavior, which is characteristic of highly accessible and active electrode surfaces. The enhanced electrochemical performance of the $MnMoO_4$/CNF/GCE electrode is thus attributed to the effective synergy between $MnMoO_4$'s redox capability and CNF's conductive network, leading to superior charge transfer efficiency and electrocatalytic activity.

3.9. Proposed Electrochemical Oxidation Mechanism of Nimesulide. The plausible electrochemical oxidation mechanism of nimesulide at the $MnMoO_4$/CNF-modified electrode is illustrated in Scheme 3. Nimesulide, a nonsteroidal anti-inflammatory drug (NSAID), contains an electron-rich aniline moiety and a nitro-substituted aromatic sulfonamide group, which are electrochemically active and can undergo redox transformations. The oxidation process is believed to initiate at the para-nitro group ($-NO_2$) attached to the aromatic ring. This group undergoes a two-electron, two-proton transfer resulting in the formation of a nitroso intermediate ($-NO$). This is further oxidized to the corresponding hydroxylamine derivative ($-NHOH$), followed by the final conversion to the highly electroactive nitrenium ion or its conjugated derivative. Simultaneously, the sulfonamide group may also contribute to the redox behavior through the formation of resonance-stabilized intermediates. The presence of $MnMoO_4$ on the electrode surface significantly enhances this multistep oxidation by providing abundant active sites and facilitating rapid electron transfer. The Mo^{6+}/Mo^{5+} and Mn^{3+}/Mn^{2+} redox couples in $MnMoO_4$ assist in mediating electron flow, while the conductive CNF network ensures efficient current collection. The stepwise transformation, highlighted by the circled regions in Scheme 3, indicates the specific sites of oxidation and bond rearrangement. These transformations are consistent with previously reported electrochemical pathways of aromatic nitro compounds and sulfonamide-containing drugs, confirming the electrocatalytic role of the $MnMoO_4$/CNF hybrid. This proposed mechanism aligns with the voltammetric responses observed experimentally and provides mechanistic insight into the oxidation pathway of nimesulide under the applied electrochemical conditions.[43]

3.10. Electrochemical Sensing of Nimesulide and Operational Parameter Optimization. *3.10.1. Electrocatalytic Reduction of Nimesulide at Various Electrodes.* The CV profiles for bare GCE, CNF/GCE, $MnMoO_4$/GCE, and $MnMoO_4$/CNF/GCE in nimesulide-containing PBS are shown in Figure 6A. The bare GCE displays a small and poorly defined cathodic peak with a reduction current of −5.8 μA, indicating minimal electron transfer activity and low electrochemical affinity toward nimesulide. Modification of the GCE with CNF leads to a noticeable enhancement in the cathodic current of −9.5 μA, owing to the improved electroactive surface area and the excellent conductivity of

https://doi.org/10.1021/acsabm.5c01031
ACS Appl. Bio Mater. 2025, 8, 8864−8879

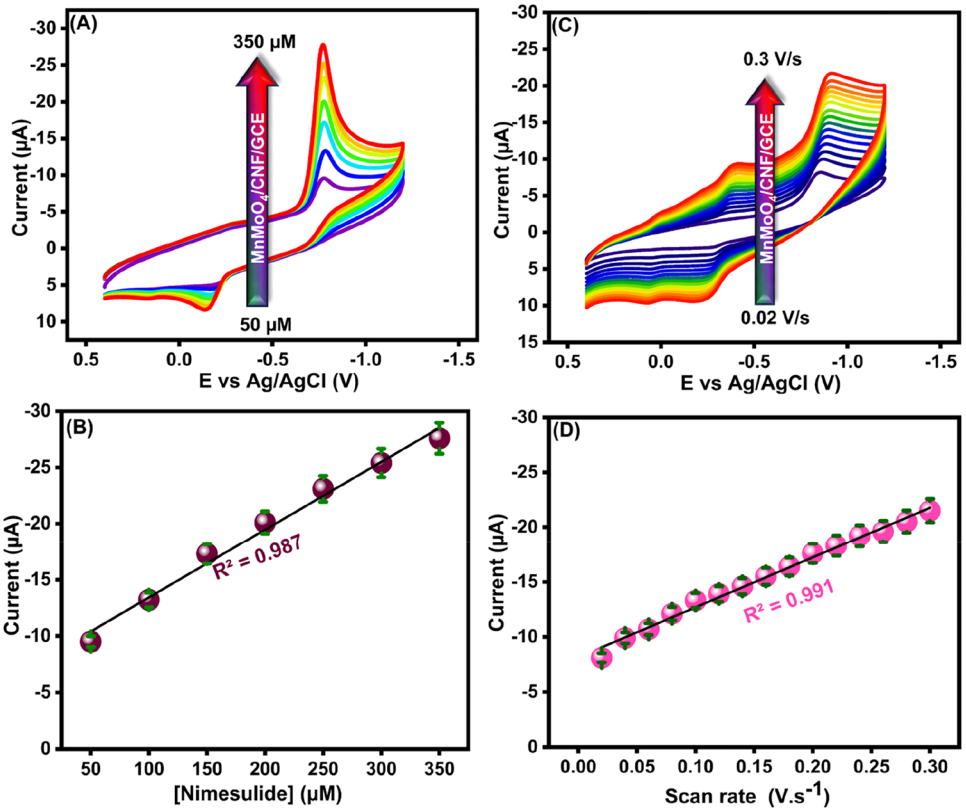

Figure 7. (A) CV analysis of $MnMoO_4$/CNF/GCE with Nimusulide concentrations from 50 to 350 μM in 0.1 M PBS. (B) Linear relationship between current response and Nimusulide concentration for $MnMoO_4$/CNF/GCE. (C) Scan rate studies of $MnMoO_4$ /CNF/GCE composite in 50 μM Nimusulide solution, varying from 0.02 to 0.3 V s^{-1}. (D) Linear graph correlating current response with scan rate for $MnMoO_4$/CNF/GCE composite.

CNFs. $MnMoO_4$-modified GCE exhibits an even stronger reduction peak of 10.9 μA, confirming the electrocatalytic nature of $MnMoO_4$, which can facilitate electron transfer through its redox-active metal centers (Mo^{6+}/Mo^{5+} and Mn^{3+}/Mn^{2+}). Notably, the $MnMoO_4$/CNF/GCE electrode demonstrates the highest cathodic current response of 13.2 μA, accompanied by a sharper and more defined peak, indicative of a faster and more reversible electrochemical reduction process. This superior performance is attributed to the synergistic effect between $MnMoO_4$ nanoparticles, which provide abundant redox-active sites, and CNFs, which offer a conductive network for efficient charge transport. A comparative summary of these current responses is plotted in Figure 6B, clearly illustrating the hierarchical enhancement due to the composite formation.

3.10.2. Optimization of $MnMoO_4$/CNF Composite Loading. The effect of varying the loading amount of the $MnMoO_4$/CNF hybrid on the electrode surface was investigated to identify the optimal configuration for maximum signal output. As illustrated in Figure 6C, increasing the loading from 2 to 6 μL/mg results in a progressive increase in cathodic current, reaching a peak value of 11.4 μA at 6 μL/mg. This is due to the increased density of electroactive material, offering more catalytic sites for nimesulide reduction. However, a further increase to 8 μL/mg causes a slight decline in current intensity 9.6 μA, which can be attributed to the excessive accumulation of the composite on the electrode surface. This excess can lead to partial blockage of the active area, limited ion diffusion, and increased resistance due to the agglomeration of particles, thereby diminishing overall electrocatalytic efficiency. The trend is quantified in Figure 6D, indicating that 6 μL/mg is the optimal loading amount that balances material availability with structural porosity and conductivity for optimal electrochemical performance.

3.10.3. Influence of pH on Nimesulide Reduction. The pH of the electrolyte plays a critical role in the redox behavior of nimesulide, particularly due to its proton-coupled electron transfer mechanism. The electrochemical response of $MnMoO_4$/CNF/GCE was evaluated across a wide pH range (3 to 11), as shown in Figure 6E.

At lower pH values (pH 3 and pH 5), the current response increases due to the availability of protons that facilitate the reduction of the electron-deficient nitro group in nimesulide. The peak current reaches its maximum at pH 7 (17.4 μA), suggesting an optimal balance between proton availability and analyte stability under physiological conditions. Beyond pH 7, the current response decreases, with values at pH 9 and pH 11 dropping to 10.4 μA and 7.3 μA, respectively. This attenuation may be due to deprotonation of active sites on the analyte or the electrode surface, or a shift in the analyte's speciation, leading to lower electrochemical reactivity. The pH-dependent variation in current response is summarized in Figure 6F, confirming that neutral to mildly acidic conditions are most favorable for efficient electron transfer and maximum signal output in nimesulide detection.

3.11. Analytical Performance of $MnMoO_4$/CNF/GCE toward Nimesulide Detection. The electrochemical sensing behavior of the $MnMoO_4$/CNF/GCE was systematically evaluated for the detection of nimesulide using CV in 0.1 M phosphate-buffered saline (PBS, pH 7.0). The investigation included assessment of the concentration-dependent response

https://doi.org/10.1021/acsabm.5c01031
ACS Appl. Bio Mater. 2025, 8, 8864−8879

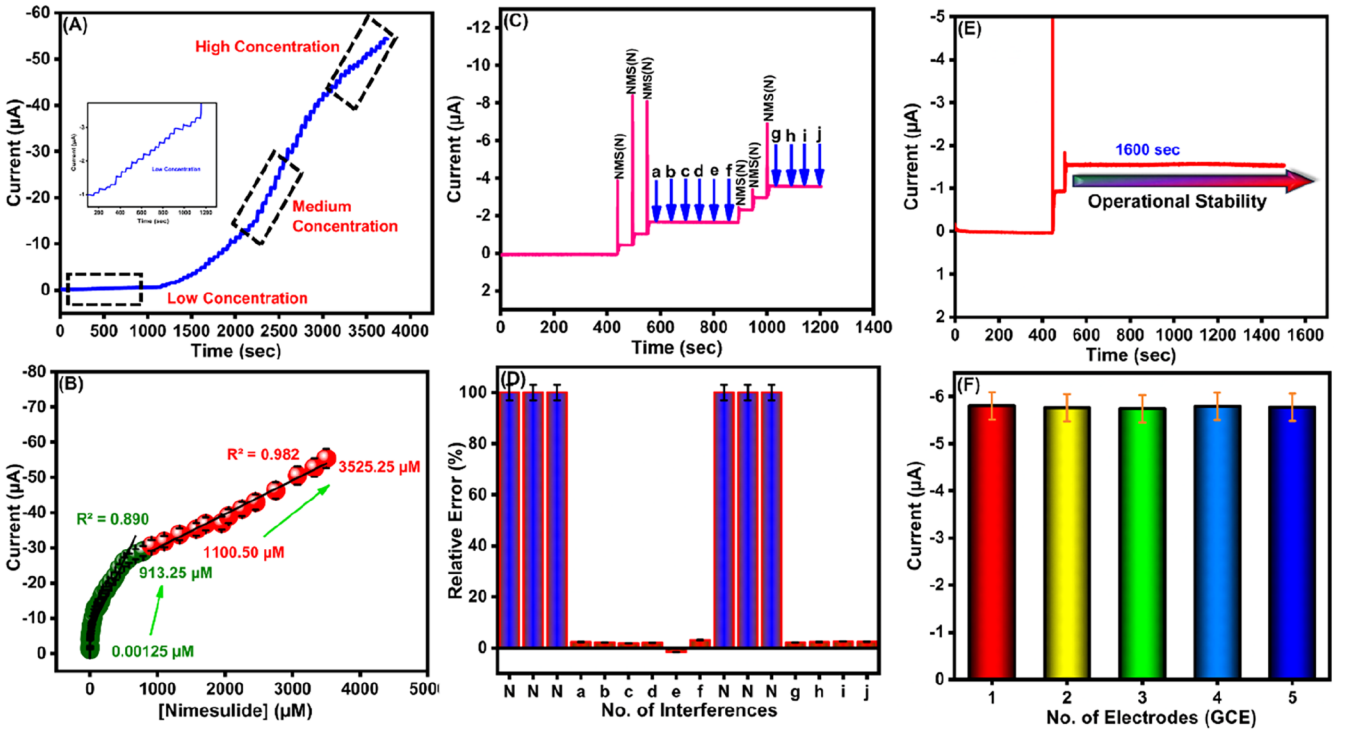

Figure 8. (A) Amperometric (i–t) analysis for $MnMoO_4$/CNF/RDE with Nimusulide concentrations ranging from 0.00125 to 3525.25 μM. (B) Linear graph showing the i–t response to varying Nimusulide concentrations for $MnMoO_4$/CNF/RDE. (C) Selectivity tests of $MnMoO_4$/CNF/RDE for Nimusulide detection in the presence of interfering compounds (a-4-nitropenol, b-dopamine, c-2-nitrophenol, d-ibuprofen, e-glucose, f-sulfadiazine, g-uric acid, h-ascorbic acid, i-nitrofurazone, j-H_2O_2). (D) Plot illustrating selectivity data from (C), comparing current responses. (E) Stability assessment of $MnMoO_4$ /CNF/RDE. (F) Bar diagram showcasing reproducibility of the $MnMoO_4$/CNF/GCE sensor across different electrodes.

and redox kinetics under varying scan rates to establish both sensitivity and the nature of the electron transfer process. The results are illustrated in Figure 7A–D.

3.11.1. Concentration-Dependent CV Response. Figure 7A shows the CV profiles recorded for the $MnMoO_4$/CNF/GCE in the presence of nimesulide concentrations ranging from 50 to 350 μM. A pronounced and progressive increase in cathodic peak current was observed with increasing analyte concentration, accompanied by a consistent peak potential shift, suggesting efficient electrocatalytic reduction of nimesulide at the modified surface. The enhancement in current can be ascribed to the higher number of electroactive nimesulide molecules being adsorbed and reduced at the catalytic $MnMoO_4$/CNF surface. The corresponding calibration curve presented in Figure 7B was constructed to evaluate the reproducibility of the sensor response toward nimesulide, using five independently fabricated electrodes (n = 5). Also, this exhibits a strong linear relationship between peak current (I) and nimesulide concentration (C), fitted to the regression equation I (μA) = [0.06036] × C + [0.00305], with a high correlation coefficient (R^2 = 0.987), confirming the reliability and linearity of the sensor response within this concentration range.

3.11.2. Electrochemical Kinetic Investigation via Scan Rate Studies. To further elucidate the electrochemical behavior and kinetics of nimesulide reduction, CVs were recorded for $MnMoO_4$/CNF/GCE in a fixed nimesulide concentration (50 μM) at various scan rates ranging from 0.02 to 0.3 V s^{-1} (Figure 7C). The peak current showed a consistent and linear increase with scan rate, while the shape of the voltammograms remained stable, suggesting a kinetically favorable and surface-confined process. This behavior was quantified in Figure 7D, where the plot of cathodic current versus scan rate yielded a linear regression with an R^2 value of 0.991. This strong linearity indicates that the redox process is predominantly adsorption-controlled, rather than governed by diffusion, which is consistent with the high surface activity and porous architecture of the $MnMoO_4$/CNF hybrid. The redox-active centers (Mo^{6+}/Mo^{5+} and Mn^{3+}/Mn^{2+}) on $MnMoO_4$, coupled with the high surface area and conductive pathways provided by CNF, facilitate rapid electron shuttling and efficient electrochemical interaction with nimesulide molecules.

3.12. Amperometric Sensing Performance, Selectivity, Operational Stability, and Reproducibility.

3.12.1. Broad-Range Amperometric Detection. Amperometric measurements (i–t curves) were performed by stepwise addition of nimesulide into a stirred 0.1 M PBS solution while applying a fixed reduction potential using a $MnMoO_4$/CNF-modified rotating disk electrode ($MnMoO_4$/CNF/RDE). As shown in Figure 8A, the current response increased proportionally with successive additions of nimesulide over a wide concentration range of 0.00125 to 3525.25 μM. The sensor exhibited three distinct linear regimes corresponding to low, medium, and high analyte concentrations, indicating dynamic surface recognition capabilities and efficient electron transfer throughout. The peaks corresponding to low concentrations of nimesulide are clearly visible in the supporting data presented in Figure S4. This figure demonstrates the sensor's excellent sensitivity and its capability to detect nimesulide even at very low concentration levels. The calibration plot in Figure 8B Reproducibility under a wide concentration range was also

https://doi.org/10.1021/acsabm.5c01031
ACS Appl. Bio Mater. 2025, 8, 8864–8879

Table 1. Comparing the Parameters of Previous Electrochemical Sensors for the Detection of Nimesulide[a]

S. No.	electrode	method	linear range (μM)	LOD (μM)	sensitivity	refs
1	cysteic acid/CNTs/GCE	DPV	0.1−10	0.05	1.0×10^{-5} A V^{-1}	44
2	Graphene paste electrode	SWV	0.5−9	0.0023		45
3	MWCNTs/GCE	LSV	0.3−65	0.16		46
4	GR/p(L-Cys)/GCE	DPV	1−55	0.3		47
5	GCE/MWCNT	CV	10−250	0.0016		48
6	$ZnFe_2O_4$/GCE	DPV	0.001−166	0.006	0.625 μA μM^{-1} cm^{-2}	49
7	Zn_2GeO_4/GCN/GCE	DPV	0.049−94.9	0.0027	5.3 μA μM^{-1} cm^{-2}	43
8	PrW-modified SPCE	i−t	0.001−131.53	0.007		50
9	TiO_2/GCE	DPV	0.1−40	0.0034		51
10	CB-Nafion/GCE	DPV	0.25−1.75	0.06		52
11	**$MnMoO_4$/CNF/GCE**	**i−t**	**0.00125−3525.25**	**0.0026**	**1.27 μA μM^{-1} cm^{-2}**	**This work**

[a]CNTs-Carbon nanotubes, GCE-glassy carbon electrodes, MWCNTs-multi wallet carbon nano tubes, GR-graphene composite, (L-Cys)-poly(L-cysteine), $ZnFe_2O_4$-zinc ferrite nanoparticles, Zn_2GeO_4-zinc germanate, GCN-graphitic carbon nitride, PrW-praseodymium tungstate, SPCE-screen-printed electrodes, TiO_2-titanium oxide, CB-carbon black.

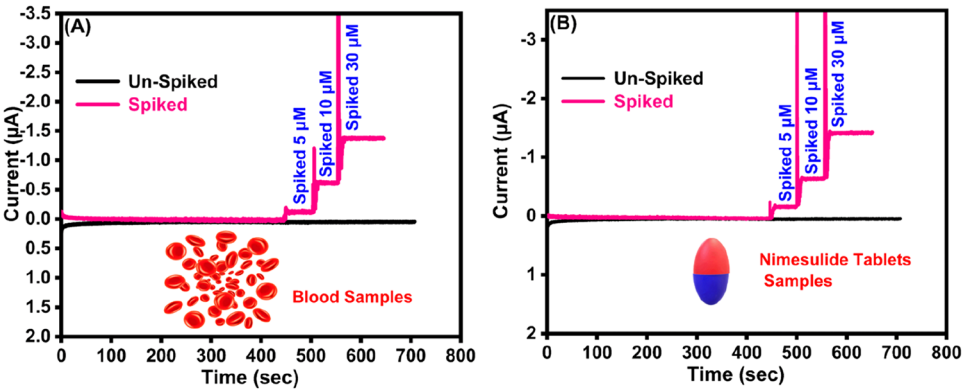

Figure 9. (A) Real sample analysis of $MnMoO_4$/CNF/GCE with Blood samples presents of Nimusulide (Spiked) and unspiked. (B) Real sample analysis of $MnMoO_4$/CNF/GCE with Nimusulide tablets presents Nimusulide (Spiked) and unspiked.

examined by testing the sensor at nimesulide (50 μM) using five independently fabricated electrodes (n = 5). Also, biphasic linear response with regression coefficients of R^2 = 0.890 (for the low concentration region, 0.00125−913.25 μM) and R^2 = 0.982 (for the higher range, 1100.50−3525.25 μM). This extended detection window demonstrates the sensor's capacity to operate effectively across diverse concentration regimes, ranging from trace environmental exposure levels to higher pharmaceutical dosages. The strong linearity at high concentrations also reflects the sensor's tolerance to surface saturation effects, owing to the composite's high surface area and porous morphology. From the slope of the calibration plot, the sensitivity of the sensor was calculated to be 1.27 μA μM^{-1} cm^{-2}, indicating a strong current response per unit concentration of analyte. Using the standard $3\sigma/S$ criterion, where σ is the standard deviation of the blank signal and S is the slope of the calibration curve, the LOD was estimated to be 0.0026 μM. These values highlight the capability of the $MnMoO_4$/CNF/RDE electrode for trace-level detection of nimesulide in aqueous media.

3.12.2. Selectivity in the Presence of Potential Interferents. To assess the selectivity of the $MnMoO_4$/CNF/RDE toward nimesulide, amperometric responses were measured in the presence of several commonly coexisting electroactive and pharmaceutical compounds. As shown in Figure 8C, the addition of nimesulide produced consistent and distinct reduction signals, while structurally similar or biologically relevant interferents, such as 4-nitrophenol (a), dopamine (b), 2-nitrophenol (c), ibuprofen (d), glucose (e), sulfadiazine (f), uric acid (g), ascorbic acid (h), nitrofurazone (i), and hydrogen peroxide (j), elicited negligible responses under identical conditions. The corresponding error analysis (Figure 8D) revealed near-zero relative error (96.6%) for all interferents, confirming that their presence does not compromise nimesulide's electrochemical recognition or catalytic reduction. This high degree of selectivity may be attributed to specific interactions between the sulfonanilide functional group of nimesulide and the active Mn and Mo sites, in combination with favorable $\pi-\pi$ stacking or hydrogen bonding interactions on the CNF-modified surface.

3.12.3. Operational Stability Assessment. The temporal stability of the $MnMoO_4$/CNF/RDE sensor was evaluated by recording the current response over 1600 s in a fixed concentration of nimesulide. As depicted in Figure 8E, the current remained nearly constant throughout the measurement period, exhibiting negligible baseline drift or degradation in the response signal. This robust performance is indicative of the excellent electrochemical and mechanical stability of the composite under prolonged operational conditions. The sustained activity may be credited to the strong anchoring of $MnMoO_4$ nanoparticles on the CNF surface, along with the chemical resilience of the Mn−O and Mo−O coordination frameworks.

3.12.4. Reproducibility Across Independently Prepared Electrodes. To assess the reproducibility of the sensor fabrication process, five $MnMoO_4$/CNF/GCE electrodes

https://doi.org/10.1021/acsabm.5c01031
ACS Appl. Bio Mater. 2025, 8, 8864−8879

were independently prepared under identical conditions and tested for their response toward a fixed 50 μM nimesulide concentration. As shown in Figure 8F, all five electrodes produced highly consistent cathodic current responses with minimal deviation, indicating excellent batch-to-batch uniformity. The calculated RSD was RSD 98.3% value further demonstrating the reliability and reproducibility of the electrode fabrication protocol. Table 1 presents a comparison of previous electrochemical sensors for the detection of nimesulide.

3.13. Real Sample Analysis for Nimesulide Detection.

To validate the analytical practicality of the $MnMoO_4$/CNF-modified electrode for real-world applications, amperometric detection studies were conducted using two representative matrices: human blood samples and commercial nimesulide tablet formulations. Both unspiked and spiked samples were tested under optimized conditions using a standard phosphate-buffered electrolyte (0.1 M PBS, pH 7.0).

3.13.1. Detection of Nimesulide in Human Blood Samples. Whole human blood was collected from healthy adult donors using EDTA-coated vacutainer tubes. The blood was immediately centrifuged at 4000 rpm for 10 min to separate plasma. The obtained plasma was diluted 10-fold with PBS (0.1 M, pH 7.0) to reduce viscosity and matrix complexity. For recovery studies, the plasma was spiked with known concentrations of nimesulide (5 μM, 10 μM, and 30 μM). The unspiked sample served as the negative control. As shown in Figure 9A, the unspiked blood sample produced negligible current, confirming the absence of endogenous nimesulide and establishing the sensor's low background signal in complex biological fluids. Upon successive spiking, sharp and well-defined stepwise increases in cathodic current were observed, indicating a direct and quantitative response to increasing analyte concentration. The sensor displayed excellent signal recovery and minimal interference from blood constituents, highlighting its high selectivity, antifouling surface characteristics, and compatibility with biological matrices.

3.13.2. Detection of Nimesulide in Pharmaceutical Tablet Samples. Commercially available nimesulide tablets (labeled content: 100 mg/tablet) were finely ground using a mortar and pestle. An accurately weighed portion (equivalent to 10 mg of nimesulide) was dissolved in 10 mL of PBS (0.1 M, pH 7.0), followed by ultrasonication for 15 min to ensure complete dissolution. The solution was filtered through a 0.22 μm syringe filter to remove insoluble excipients. The filtrate was used as the stock tablet extract. Aliquots were spiked with standard nimesulide solutions (5, 10, and 30 μM) to assess recovery and matrix effects. Unspiked filtrates were used as controls. As depicted in Figure 9B, no significant current response was observed in the unspiked tablet extract, suggesting minimal electrochemical interference from excipients or inactive ingredients. Upon incremental spiking, the current increased proportionally with each concentration step, displaying sharp and consistent transitions. This reflects the sensor's robust signal transduction even in the presence of potentially interfering formulation components. Table 2. The recovery rates obtained for the Blood and Tablet samples fell within the ranges of ~99%, respectively, showcasing the sensor's high efficacy in detecting and quantifying nimesulide in complex matrices typically found in Blood and Tablet samples.

Table 2. Recovery Rates Obtained for the Blood and Tablet Samples

samples	added (μM)	$i-t$ found (μM)	recovery (%) (n = 3) ± RSD
blood	5	4.92	98.4 ± 0.21
	10	9.92	99.2 ± 0.15
	30	29.47	98.2 ± 0.32
nimesulide tablet	5	4.85	98.2 ± 0.18
	10	9.91	99.1 ± 0.22
	30	28.9	98.9 ± 0.23

4. CONCLUSIONS

In this study, a $MnMoO_4$/CNF hybrid composite was successfully synthesized via a deep eutectic solvent-assisted hydrothermal approach and employed as an efficient electrocatalyst for the electrochemical detection of nimesulide. Comprehensive structural, morphological, and surface characterizations confirmed the formation of well-crystallized $MnMoO_4$ nanoparticles uniformly anchored on the functionalized CNF matrix, resulting in increased surface area, enhanced electron transport, and improved redox activity. The $MnMoO_4$/CNF-modified electrode exhibited outstanding electroanalytical performance, characterized by a broad linear detection range (0.00125−3525.25 μM), a low limit of detection (0.0026 μM), high sensitivity (1.27 μA μM^{-1} cm^{-2}), and adsorption-controlled electrochemical kinetics. The sensor demonstrated excellent selectivity against structurally and electrochemically analogous interferents, along with superior operational stability and reproducible fabrication. Its applicability was further validated through the successful detection of nimesulide in spiked human blood and commercial pharmaceutical formulations, confirming its robustness in complex real-world matrices. The synergistic interaction between redox-active $MnMoO_4$ and the highly conductive CNFs is central to the sensor's enhanced sensitivity and stability, positioning this composite as a promising candidate for point-of-care diagnostics, therapeutic drug monitoring, and pharmaceutical quality control. Future efforts may focus on sensor miniaturization and integration with portable platforms for real-time on-site monitoring.

■ ASSOCIATED CONTENT

Supporting Information

The Supporting Information is available free of charge at https://pubs.acs.org/doi/10.1021/acsabm.5c01031.

Details of chemicals, instrumentation, and electrochemical setup (Section S1); XPS spectrum of $MnMoO_4$/CNF (Figure S1); FESEM and EDX analysis of $MnMoO_4$/CNF (Figure S2); TEM and EDX mapping of $MnMoO_4$/CNF composite (Figure S3); amperometric detection of nimesulide (Figure S4) (PDF)

■ AUTHOR INFORMATION

Corresponding Authors

Yung-Lung Chen − *Division of Cardiology, Department of Internal Medicine, Kaohsiung Chang Gung Memorial Hospital, College of Medicine, Chang Gung University, Kaohsiung 833, Taiwan; Graduate Institute of Clinical Medical Sciences, College of Medicine, Chang Gung*

https://doi.org/10.1021/acsabm.5c01031
ACS Appl. Bio Mater. 2025, 8, 8864−8879

University, Taoyuan 333, Taiwan; Email: feymanchen@gmail.com

Kun-Mu Lee − *Department of Chemical and Materials Engineering, Chang Gung University, Taoyuan 33302, Taiwan; Center for Sustainability and Energy Technologies, Chang Gung University, Taoyuan 33302, Taiwan; Division of Neonatology, Department of Pediatrics, Chang Gung Memorial Hospital, Taoyuan 33305, Taiwan; College of Environment and Resources, Ming Chi University of Technology, New Taipei City 24301, Taiwan;* orcid.org/0000-0002-5911-9386; Email: kmlee@mail.cgu.edu.tw

Authors

Kumar Gokulkumar − *Department of Chemical and Materials Engineering, Chang Gung University, Taoyuan 33302, Taiwan;* orcid.org/0009-0008-1944-7116

Sakthivel Kogularasu − *Super Micro Mass Research and Technology Center, Cheng Shiu University, Kaohsiung 833301, Taiwan; Center for Environmental Toxin and Emerging-Contaminant Research and Institute of Environmental Toxin and Emerging Contaminant, Cheng Shiu University, Kaohsiung 833301, Taiwan;* orcid.org/0000-0002-4606-3846

Shih-Hsuan Chen − *Department of Chemical and Materials Engineering, Chang Gung University, Taoyuan 33302, Taiwan*

Guo-Ping Chang-Chien − *Super Micro Mass Research and Technology Center, Cheng Shiu University, Kaohsiung 833301, Taiwan; Center for Environmental Toxin and Emerging-Contaminant Research and Institute of Environmental Toxin and Emerging Contaminant, Cheng Shiu University, Kaohsiung 833301, Taiwan*

Wan-Ching Lin − *Department of Neuroradiology, E-da Hospital, I-Shou University, Kaohsiung 84001, Taiwan; Department of Neurosurgery, E-Da Hospital, I-Shou University, Kaohsiung 84001, Taiwan*

Complete contact information is available at: https://pubs.acs.org/10.1021/acsabm.5c01031

Notes

The authors declare no competing financial interest.

■ ACKNOWLEDGMENTS

This research investigation is supported by the National Science and Technology Council, Taiwan (111-2223-E-182-001-MY4), Chang Gung University (URRPD2Q0041), Chang Gung Memorial Hospital, Linkou, Taiwan (CMRPD2M0042), and Cheng Shiu University, Taiwan.

■ REFERENCES

(1) Sharma, J.; Joshi, M.; Bhatnagar, A.; Chaurasia, A. K.; Nigam, S. Pharmaceutical residues: One of the significant problems in achieving 'clean water for all'and its solution. *Environ. Res.* **2022**, *215*, No. 114219.

(2) Adedipe, D. T.; Chen, C.; Lai, R. W. S.; Xu, S.; Luo, Q.; Zhou, G.-J.; Boxall, A.; Brooks, B. W.; Doblin, M. A.; Wang, X.; et al. Occurrence and potential risks of pharmaceutical contamination in global Estuaries: A critical review and analysis. *Environ. Int.* **2024**, *192*, No. 109031.

(3) Michelangeli, M.; Martin, J. M.; Robson, S.; Cerveny, D.; Walsh, R.; Richmond, E. K.; Grace, M. R.; Brand, J. A.; Bertram, M. G.; Ho, S. S.; et al. Pharmaceutical pollution alters the structure of freshwater communities and hinders their recovery from a fish predator. *Environ. Sci. Technol.* **2024**, *58* (31), 13904−13917.

(4) Matesun, J.; Petrik, L.; Musvoto, E.; Ayinde, W.; Ikumi, D. Limitations of wastewater treatment plants in removing trace anthropogenic biomarkers and future directions: A review. *Ecotoxicol. Environ. Saf.* **2024**, *281*, No. 116610.

(5) Mezzelani, M.; Gorbi, S.; Da Ros, Z.; Fattorini, D.; d'Errico, G.; Milan, M.; Bargelloni, L.; Regoli, F. Ecotoxicological potential of non-steroidal anti-inflammatory drugs (NSAIDs) in marine organisms: bioavailability, biomarkers and natural occurrence in Mytilus galloprovincialis. *Mar. Environ. Res.* **2016**, *121*, 31−39.

(6) de Carvalho, W. F.; de Souza Pereira Lima, E.; de Castro, W. V.; Thomé, R. G.; Santos, H. B. Toxicological effect of acetaminophen, metamizole, and nimesulide cocktail on early development of zebrafish. *DARU Jo. Pharm. Sci.* **2024**, *32* (2), 585−597.

(7) Yu, L.; Lin, Y.; Li, J.; Deng, C.; Zhang, R.; Liu, A.; Wang, L.; Li, Y.; Wei, X.; Lu, D.; et al. Suspect Screening of Pharmaceuticals and Their Transformation Products (TPs) in Wastewater during COVID-19 Infection Peak: Identification of New TPs and Elevated Risks. *Environ. Sci. Technol.* **2025**, *59* (10), 4893−4905.

(8) Jagirani, M. S.; Soylak, M. A review: Recent advances in solid phase microextraction of toxic pollutants using nanotechnology scenario. *Microchem. J.* **2020**, *159*, No. 105436.

(9) Jagirani, M. S.; Soylak, M. Metal-organic framework nanosheets (MONs) a breakthrough in separation and pre-concentration technique: A review. *TrAC, Trends Anal. Chem.* **2024**, *178*, No. 117838.

(10) Khan, W. A.; Arain, M. B.; Balal, S.; Mollahosseini, A.; Soylak, M. Deep eutectic solvent-functionalized metal-organic frameworks in sorptive extraction techniques and their applications−A review. *Microchem. J.* **2025**, *212*, No. 113201.

(11) Gokulkumar, K.; Huang, S.-J.; Lee, Y.-Y.; Kogularasu, S.; Chang-Chien, G.-P. Nanoparticles of SnS on carbon nanofibers for electrochemical detection of vanillin. *ACS Appl. Nano Mater.* **2024**, *7* (11), 13183−13193.

(12) Sriram, B.; Kogularasu, S.; Wang, S.-F.; Chang-Chien, G.-P. Electrochemical Detection of Synthetic Vanillin Using a Strontium Pyrophosphate Nanorod-Modified Electrode. *ACS Mater. Au* **2025**, *5*, 632−640.

(13) Velraj, A.; Sivaji, S. P.; Chen, S.-M.; Bharath, G.; Chiesa, M.; Liu, J.-T. Fruitful design of novel SrV2O6@ MCM-41-based electrochemical sensor for carcinogenic carbendazim detection in complex real-world matrices. *Composites, Part B* **2025**, *300*, No. 112475.

(14) Kogularasu, S.; Sriram, B.; Wang, S.-F.; Lin, W.-C.; Lee, Y.-Y.; Chen, Y.-L.; Chang-Chien, G.-P. Sustainable Synthesis of Rare Earth Metal Tungstates (REWO, RE= Ce, SM, Gd) for Electrochemical Detection of 4-Nitrotoluene. *ACS Eng. Au* **2024**, *4* (6), 533−544.

(15) Gokulkumar, K.; Priscillal, I. J. D.; Wang, S.-F. Deep eutectic solvent-mediated synthesis of PDA coated f-CNF doped ZnS nanoparticles for electrode modification: Innovative sensing platform for determination of pollutant 3-nitrophenol. *J. Alloys Compd.* **2022**, *924*, No. 166561.

(16) Manimaran, P.; Tamilalagan, E.; Chen, S.-M.; Govindharaj, A. Development of an ultrasensitive sensor for detecting metol in environmental water samples using ruddlesden-popper type layered perovskite (La2NiO4) combined with graphene oxide. *Water Res.* **2025**, *273*, No. 122998.

(17) Kuang, J.; Yan, S.; Housel, L. M.; Ehrlich, S. N.; Ma, L.; Takeuchi, K. J.; Takeuchi, E. S.; Marschilok, A. C.; Wang, L. Manganese Molybdate Cathodes with Dual-Redox Centers for Aqueous Zinc-Ion Batteries: Impact of Electrolyte on Electrochemistry. *ACS Sustainable Chem. Eng.* **2022**, *10* (49), 16197−16213.

(18) Khan, M. I.; Mujtaba, A.; Alshahrani, D. O.; Ezzine, S.; Islam, G. U. Electrochemical properties of MnMoO 4 nanoparticles for energy storage applications synthesized via a green approach using Camellia sinensis extract as a reducing and stabilizing agent. *New J. Chem.* **2025**, *49* (3), 1053−1061.

(19) Baby, J. N.; Sriram, B.; Wang, S.-F.; George, M.; Govindasamy, M.; Joseph, X. B. Deep eutectic solvent-based manganese molybdate nanosheets for sensitive and simultaneous detection of human lethal

compounds: comparing the electrochemical performances of M-molybdate (M= Mg, Fe, and Mn) electrocatalysts. *Nanoscale* **2020**, *12* (38), 19719−19731.
(20) Rajput, A.; Kumari, A.; Basak, H. K.; Ghosh, D.; Chakraborty, B. Tracking the active phase and reaction pathway of the OER mediated by an MnMoO 4 microrod electro (pre)-catalyst. *J. Mater. Chem. A* **2024**, *12* (44), 30810−30820.
(21) da Silveira Lacerda, L. H.; San-Miguel, M. A. Unraveling the MnMoO4 polymorphism: a comprehensive DFT investigation of α, β, and ω phases. *J. Mater. Sci.* **2022**, *57* (22), 10179−10196.
(22) Yadava, Y.; Singh, R. Electrical conduction in manganese molybdate. *Mater. Chem. Phys.* **1987**, *17* (3), 259−272.
(23) Gokulkumar, K.; Huang, S.-J.; Wang, S.-F.; Balaji, R.; Chandrasekar, N.; Hwang, M. T. Zinc molybdate/functionalized carbon nanofiber composites modified electrodes for high-performance amperometric detection of hazardous drug Sulfadiazine. *OpenNano* **2023**, *10*, No. 100131.
(24) Huang, S.-J.; Gokulkumar, K.; Mani, G.; lee, Y. Y.; Kogularasu, S.; Chang-Chien, G.-P. Synthesis and characterization of Bi2S3-embedded carbon nanofibers as a novel electrochemical biosensor for the detection of mycotoxin zearalenone in food crops. *FlatChem* **2024**, *45*, No. 100652.
(25) Zou, G.; Zhang, D.; Dong, C.; Li, H.; Xiong, K.; Fei, L.; Qian, Y. Carbon nanofibers: Synthesis, characterization, and electrochemical properties. *Carbon* **2006**, *44* (5), 828−832.
(26) Jeon, D.; Sagong, M.; Kim, M. S.; Nam, J. S.; Park, H.; Kim, I. D. Electrospun Carbon Nanofibers for Clean Energy Applications: A Comprehensive Review. *EcoMat* **2025**, *7* (2), No. e12517.
(27) Ahmad, M. W.; Anand, S.; Shalini, K.; Ul-Islam, M.; Yang, D.-J.; Choudhury, A. MnMoO4 nanorods-encapsulated carbon nanofibers hybrid mat as binder-free electrode for flexible asymmetric supercapacitors. *Mater. Sci. Semicond. Process.* **2021**, *136*, No. 106176.
(28) Suo, G.; Cheng, Y.; Mu, R.; Hou, X.; Yang, Y.; Ye, X.; Zhang, L. Bimetallic MnMoO4 nanostructures on carbon fibers as flexible cathode for high performance zinc-ion batteries. *J. Colloid Interface Sci.* **2023**, *641*, 981−989.
(29) Zhou, Y.; Li, Q.; Lu, T.; Zhang, Y.; He, W.; Zhang, E.; Liu, C.; Wang, X.; Li, Z.; Zhu, Y.; Xu, B. Rational Design of Three-Dimensional Architectures of Carbon Nanorods/Carbon Nanofibers Composite for High-Performance Supercapacitors. *ACS Appl. Energy Mater.* **2025**, *8*, 1414−1419.
(30) Kundu, A.; Shetti, N. P.; Basu, S.; Mondal, K.; Sharma, A.; Aminabhavi, T. M. Versatile carbon nanofiber-based sensors. *ACS Appl. Bio Mater.* **2022**, *5* (9), 4086−4102.
(31) Wang, T.; Chen, Z.; Gong, W.; Xu, F.; Song, X.; He, X.; Fan, M. Electrospun carbon nanofibers and their applications in several areas. *ACS Omega* **2023**, *8* (25), 22316−22330.
(32) Venkatesh, K.; Rajakumaran, R.; Chen, S.-M.; Karuppiah, C.; Yang, C.-C.; Ramaraj, S. K.; Ali, M. A.; Al-Hemaid, F. M.; El-Shikh, M. S.; Almunqedhi, B. A novel hybrid construction of MnMoO4 nanorods anchored graphene nanosheets; an efficient electrocatalyst for the picomolar detection of ecological pollutant ornidazole in water and urine samples. *Chemosphere* **2021**, *273*, No. 129665.
(33) Govindharaj, A.; Manimaran, P.; Chen, S.-M.; Tamilalagan, E.; Selvaraj, M.; Singh, G. An electrochemical signal amplification using functionalized carbon nanofiber integrated manganese molybdate nanocomposite for rapid detection of vanillin in food samples. *Food Chem.* **2025**, *475*, No. 143334.
(34) Gokulkumar, K.; Huang, S.-J.; Kogularasu, S.; Aljuwayid, A. M.; Maheshwaran, S.; Govindasamy, M. Enhanced electrochemical detection of tartrazine in beverages and liquid soap via nickel phosphide-adorned functionalized carbon nanofibers. *J. Taiwan Inst. Chem. Eng.* **2024**, *157*, No. 105420.
(35) Priscillal, I. J. D.; Wang, S.-F. Synchronously activated strontium aluminate nanoflakes anchored functionalized carbon nanofiber nanocomposite for sensitive amperometric detection of food additive: Propyl gallate. *Food Chem.* **2022**, *389*, No. 133119.
(36) Zhao, Q.-L.; Bao, L.; Luo, Q.-Y.; Zhang, M.; Lin, Y.; Pang, D.-W.; Zhang, Z.-L. Surface manipulation for improving the sensitivity and selectivity of glassy carbon electrodes by electrochemical treatment. *Biosens. Bioelectron.* **2009**, *24* (10), 3003−3007.
(37) Zhu, X.; Chen, Y.; Feng, C.; Wang, W.; Bo, B.; Ren, R.; Li, G. Assembly of self-cleaning electrode surface for the development of refreshable biosensors. *Anal. Chem.* **2017**, *89* (7), 4131−4138.
(38) Mutharani, B.; Ranganathan, P.; Chang, Y.-H.; Chiu, F.-C. Design of lignin-wrapped stable liquid GaInSn conductive ink for high-sensitivity electrochemical detection of nimesulide. *Chem. Eng. J.* **2025**, *509*, No. 161379.
(39) Harichandran, G.; Radha, S.; Divya, P.; Yesuraj, J. Facile morphology-controlled synthesis of nanostructured MnMoO 4 nanorods as an advance electrode material for supercapacitor application. *J. Mater. Sci.: Mater. Electron.* **2020**, *31*, 1646−1653.
(40) Lu, Y.; Zhao, M.; Luo, R.; Yu, Q.; Lv, J.; Wang, W.; Yan, H.; Peng, T.; Liu, X.; Luo, Y. Electrospun porous MnMoO 4 nanotubes as high-performance electrodes for asymmetric supercapacitors. *J. Solid State Electrochem.* **2018**, *22*, 657−666.
(41) Huang, S.-J.; Gokulkumar, K.; Govindasamy, M.; Albaqami, M. D.; Wabaidur, S. M. Nanoarchitectonics of europium vanadate nanoparticles decorated carbon nanofibers for electrochemical detection of fungicide in fruits. *J. Taiwan Inst. Chem. Eng.* **2024**, *161*, No. 105563.
(42) Kogularasu, S.; Govindasamy, M.; Chen, S.-M.; Akilarasan, M.; Mani, V. 3D graphene oxide-cobalt oxide polyhedrons for highly sensitive non-enzymatic electrochemical determination of hydrogen peroxide. *Sens. Actuators, B* **2017**, *253*, 773−783.
(43) Ganesamurthi, J.; Lee, D.; Muthukutty, B.; Juang, R.-S. Developing a ternary metal oxide Zn2GeO4 with graphitic carbon nitride supported nanocomposite for electrochemical assessment of nanomolar-scale nimesulide. *J. Taiwan Inst. Chem. Eng.* **2025**, *169*, No. 105986.
(44) Wang, C.; Shao, X.; Liu, Q.; Qu, Q.; Yang, G.; Hu, X. Differential pulse voltammetric determination of nimesulide in pharmaceutical formulation and human serum at glassy carbon electrode modified by cysteic acid/CNTs based on electrochemical oxidation of l-cysteine. *J. Pharm. Biomed. Anal.* **2006**, *42* (2), 237−244.
(45) Materon, E. M.; Wong, A.; Gomes, L. M.; Ibanez-Redin, G.; Joshi, N.; Oliveira, O. N.; Faria, R. C. Combining 3D printing and screen-printing in miniaturized, disposable sensors with carbon paste electrodes. *J. Mater. Chem. C* **2021**, *9* (17), 5633−5642.
(46) Zhang, J.; Tan, X.; Zhao, D.; Tan, S.; Huang, Z.; Mi, Y.; Huang, Z. Study of nimesulide and its determination using multiwalled carbon nanotubes modified glassy carbon electrodes. *Electrochim. Acta* **2010**, *55* (7), 2522−2526.
(47) Yue, X.; Xu, X.; Liu, C.; Zhao, S. Simultaneous determination of cefotaxime and nimesulide using poly (L-cysteine) and graphene composite modified glassy carbon electrode. *Microchem. J.* **2022**, *174*, No. 107058.
(48) Moscoso, R.; Álvarez-Lueje, A.; Squella, J. Nanostructured interfaces containing MWCNT and nitro aromatics: A new tool to determine Nimesulide. *Microchem. J.* **2020**, *159*, No. 105361.
(49) Anupriya, J.; Babulal, S. M.; Chen, T.-W.; Chen, S.-M.; Kumar, J. V.; Lee, J.-W.; Rwei, S.-P.; Yu, J.; Yu, R.; Hong, C.-Y. Facile hydrothermal synthesis of cubic zinc ferrite nanoparticles for electrochemical detection of anti-inflammatory drug nimesulide in biological and pharmaceutical sample. *Int. J. Electrochem. Sci.* **2021**, *16* (7), No. 210772.
(50) Sriram, B.; Sherlin, V. A.; Wang, S.-F.; George, M. Surfactant assisted synthesis of PrM through M site variants (M= Mo, V, and W) for the electrochemical detection of nonsteroidal anti-inflammatory drug−Nimesulide. *J. Mol. Liq.* **2024**, *398*, No. 124243.
(51) Bukkitgar, S. D.; Shetti, N. P.; Kulkarni, R. M.; Halbhavi, S. B.; Wasim, M.; Mylar, M.; Durgi, P. S.; Chirmure, S. S. Electrochemical oxidation of nimesulide in aqueous acid solutions based on TiO2 nanostructure modified electrode as a sensor. *J. Electroanal. Chem.* **2016**, *778*, 103−109.
(52) Łysoń, M.; Górska, A.; Paczosa-Bator, B.; Piech, R. Nimesulide determination on carbon black-nafion modified glassy carbon

https://doi.org/10.1021/acsabm.5c01031
ACS Appl. Bio Mater. 2025, 8, 8864−8879

electrode by means of adsorptive stripping voltammetry. *Electrocatalysis* **2021**, *12* (6), 641−649.

https://doi.org/10.1021/acsabm.5c01031
ACS Appl. Bio Mater. 2025, 8, 8864−8879